Experiments and Molecular Simulations to Study the Role of Coadsorption of Oil in Corrosion Inhibitor Films in Improving Corrosion Mitigation

Xueying Ko, Juan Dominguez Olivo,* Bruce Brown,* Srdjan Nešić,‡,* and Sumit Sharma‡,**

While both field experience and laboratory experiments have shown that the efficiency of adsorbed corrosion inhibitor films improves upon exposure of the aqueous solution to a hydrocarbon phase, a credible explanation of these results is lacking. Using a combination of experiments and molecular simulations, this study examines how exposure to oil molecules affects the nature of adsorbed corrosion inhibitor films on metal surfaces. It is found that oil molecules get coadsorbed in the corrosion inhibitor films, making them more hydrophobic, structurally more ordered, and well packed. Corrosion inhibitor molecules with a bulky polar head adsorb in nonplanar, cylinder-like morphologies. Coadsorption of oil molecules changes the morphology of these films to a planar self-assembled monolayer.

KEY WORDS: adsorption, corrosion inhibitors, molecular simulations

INTRODUCTION

Oil and gas transportation pipelines, made of mild steel, are prone to internal corrosion upon exposure to water, which is invariably present in oil and gas streams.[1] An efficient and cost-effective method of mitigating internal corrosion of these pipelines is to inject organic corrosion inhibitors in the fluid stream continuously at concentration levels of parts per million.[2-3] Amphiphilic surfactant molecules have been found to be effective corrosion inhibitors.[2-4] Imidazole, quaternary ammonium, amide, and amidoamine-based surfactants are popular corrosion inhibitors due to their low toxicity and high efficacy.[4-6] These molecules consist of a hydrophobic tail (nonpolar) and a hydrophilic head (polar) group. The hydrophobic tails are hydrocarbon chains comprised of usually 6 to 22 carbon atoms, while the hydrophilic heads are either non-ionic or ionic functional groups. The protective properties of these molecules are closely related to their adsorption at the metal/water interface.[7]

Adsorption behavior as well as efficiency of corrosion inhibitors have been researched extensively in experimental and simulation studies.[8-13] Most of these studies have focused on evaluating the corrosion inhibition mechanism in aqueous phase devoid of any oil. A few researchers have studied the effect of oil wetting and have reported that the presence of an oil phase improves the corrosion inhibition efficiency of inhibitor molecules.[14] McMahon showed that the adsorption of oleic imidazoline inhibitors onto oil-wet steel surfaces was fast and does not depend on the type of oil used to wet the surface. A monolayer of oleic imidazoline was found to adsorb on the oil-wet steel surface.[2] Improvement in corrosion inhibition due to oil has been reported in other studies.[15] Foss, et al., studied the effect of corrosion inhibitors on the wettability of carbon steel,[16] iron carbonate ($FeCO_3$) covered steel surfaces,[17] and ferric oxide covered steel surfaces[18] and found that both oleic imidazoline and phosphate ester altered the wettability of a bare steel surface from hydrophilic to hydrophobic, and the performance of oleic imidazoline and phosphate ester significantly increased after oil wetting of the bare steel surface and iron carbonate covered steel surface. By observing the water droplet contact angle as a function of inhibitor concentration, Li, et al.,[14] concluded that a fatty amine-type inhibitor was more effective in altering the wettability from water-wet to oil-wet compared to quaternary ammonium chloride inhibitors, and direct exposure of the surface to oil enhanced the performance of the fatty amine-type inhibitor. Researchers have attributed this improved performance to coadsorption of inhibitor and oil molecules at the metal/water interface. These experimental works provide evidence that the presence of oil has an effect on the adsorption and performance of corrosion inhibitors. So far, these experimental observations have only been explained by hypothesizing how oil molecules might be interacting with corrosion inhibitor molecules. There has been no direct investigation of the molecular-level interactions between oil and corrosion inhibitor molecules.

In this study, molecular simulations have been performed to understand how the presence of oil molecules affects the adsorption behavior of corrosion inhibitor molecules. This study reports that oil molecules get coadsorbed in the corrosion inhibitor film due to lateral hydrophobic interactions between the oil molecules and the tails of inhibitor molecules. It was found that the coadsorbed oil molecules are able to

Submitted for publication: June 5, 2020. Revised and accepted: July 29, 2020. Preprint available online: July 29, 2020, https://doi.org/10.5006/3606.
‡ Corresponding author. E-mail: sharmas@ohio.edu; nesic@ohio.edu.
* Department of Chemical and Biomolecular Engineering, Ohio University, Athens, Ohio 45701.

ISSN 0010-9312 (print), 1938-159X (online)

change the morphology of adsorbed corrosion inhibitor films and can significantly enhance the structural ordering and hydrophobic character of the adsorbed films. This is the first ever study that has directly revealed molecular-level behavior of how oil molecules affect corrosion inhibitor films.

SCOPE OF WORK

2.1 | Basic Ideas of Molecular Simulations

It is understood that any equilibrium thermodynamic state is essentially an ensemble of a large number of molecular configurations or microstates because molecules are in constant motion. To get a quantitative perspective, consider that the average speed of molecules, calculated via Maxwell-Boltzmann distribution, is approximately 500 m/s at room temperature. At liquid state densities, the mean free path between the molecules is approximately 0.5 nm, so one would expect close to 10^{12} molecular collisions occurring per second per molecule. Consequently, thermodynamic properties are statistical properties of a large number of microstates. The relationship between molecular and thermodynamic properties is well established in the theory of statistical mechanics. In molecular simulations, microstates associated with a thermodynamic state are generated by simulating the motion of molecules, often by utilizing the computational power of many processors operating in a parallel fashion in a computer cluster.

To simulate molecular motion, one needs to know the nature of atomic forces. Every atom in a system exerts a distance-dependent force on every other atom. These forces are electrostatic in nature and arise due to the interactions of electron clouds and nuclei. While calculation of electronic motion requires solving the equations of quantum mechanics, the motion of nuclei of atoms heavier than hydrogen can be well understood via classical Newtonian mechanics. The forces depend on the type of the atoms. For example, nonpolar alkane molecules will predominantly interact via van der Waals forces. Polar and charged molecules will also have coulombic interactions. Distance-dependent forces between different atoms are represented via mathematical functions called force fields.

Therefore, to perform molecular simulations, one needs to generate an initial molecular configuration of the system, define the force field, and define the thermodynamic state of the system, such as a constant number of molecules (N), volume (V), and temperature (T). Starting from the initial molecular configuration, forces between all atoms are calculated. Numerical integration of classical equations of motion is then performed to generate molecular trajectories. The forces are calculated after every femto-second (10^{-15} s) because the forces depend on the distance between the atoms and therefore are continuously changing.

2.2 | Simulation Setup

Often, a useful approach to study molecular behavior is to use a coarse-grained (CG) description of the molecules that comprise a system. In a CG description, instead of explicitly representing every atom in the simulation, a group of atoms is combined into a united atom or a CG bead, as shown schematically in Figure 1.[19] As an example, an alkyl group can be represented by only one bead. This approach helps in significantly reducing the number of particles in the simulation system and thus makes the simulation computationally fast. In systems where a large number of molecules are needed, for example, in self-assembly or phase transitions, CG descriptions are useful to enable longer simulations.

In this study, corrosion inhibitor molecules are represented by a CG model, the same as the one used in a previous study.[20] A corrosion inhibitor molecule has a polar head group, which has strong affinity for the metal surface. Alkyl tails of corrosion inhibitor molecules have hydrophobic interactions between them. In this CG model, one terminal bead represents the polar head group, and all of the other beads in the molecule are hydrophobic and represent the alkyl tail. Oil molecules are represented as linear chains of hydrophobic beads. Bonds between the connected beads in a molecule are modeled as harmonic potentials given by:

$$V_b(r) = k(r - r_0)^2 \quad (1)$$

where $V_b(r)$ is the distance-dependent bond potential, k is the bond coefficient, r is the distance between the two connected beads, and r_0 is the equilibrium bond-length. The angle between two adjacent bonds in a molecule is restrained via harmonic potentials given by:

$$V_a(\theta) = k_\theta(\theta - \theta_0)^2 \quad (2)$$

where $V_a(\theta)$ is the angle potential, k_θ is the angle coefficient, θ is the value of angle between the bonds, and θ_0 is the equilibrium angle. The equilibrium angle is set to 180° to model linear corrosion inhibitor molecules. Interactions between all hydrophobic beads, that is, between the tail beads of inhibitor molecules, between the oil beads, as well as between the inhibitor tail and oil beads, are modeled via Lennard-Jones (LJ) potential with the length parameter (σ) and potential well depth of ε:

$$V_{LJ}(r) = 4\varepsilon\left(\frac{\sigma^{12}}{r^{12}} - \frac{\sigma^6}{r^6}\right) \quad (3)$$

The potential well-depth parameter (ε) determines the strength of the attractive interaction. The parameter σ determines the effective diameter of the bead. In an LJ potential, at distances $r < 2^{1/6}\sigma$, the interaction potential becomes strongly repulsive, whereas, for distances $r > 2^{1/6}\sigma$, the potential is attractive. The LJ potential decreases at the rate of r^{-6} and therefore is a short-ranged potential. LJ potential is used to model van der Waals and hydrophobic interactions between species. Interactions between the polar head beads and the hydrophobic beads are modeled by purely repulsive

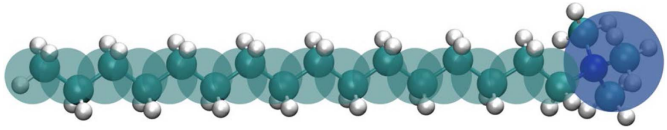

FIGURE 1. *A schematic of the coarse-grained model of a corrosion inhibitor. The cyan-colored beads represent the alkyl tail, and the blue-colored bead represents the polar head group.*

Weeks-Chandler-Anderson (WCA) potential.[21] WCA potential is a truncated and shifted LJ potential that includes only the repulsive part of LJ potential, with the LJ length parameter σ_p determining the effective diameter of the polar bead. The functional form of WCA potential is given by:

$$V_{WCA}(r) = 4\varepsilon\left(\frac{\sigma_p^{12}}{r^{12}} - \frac{\sigma_p^{6}}{r^{6}}\right) + \varepsilon \text{ for } r < 2^{1/6}\sigma_P \text{ and 0 otherwise} \quad (4)$$

In effect, the WCA potential models the excluded volume interactions between species. In an aqueous environment, polar head groups are solvated and thus do not have a net interaction with other polar head groups apart from excluded volume because of their size. The metal surface is represented by a smooth, two-dimensional surface occupying the bottom face of the simulation box at z = 0. The strong attractive interactions between the polar head beads and the surface are modeled via a 9-3 potential with the well depth of ε_s. A 9-3 potential represents the net interaction due to a semi-infinite slab made of LJ particles.[22] The functional form of 9-3 potential is given by:

$$V_{9\text{-}3}(z) = \varepsilon_S\left(\frac{2}{15}\frac{\sigma_S^9}{z^9} - \frac{\sigma_S^3}{z^3}\right) \quad (5)$$

where z is the distance from the surface. The hydrophobic beads have only repulsive, hard sphere interactions with the surface. Water is treated implicitly in the simulation. The effect of water is taken into account by including an attractive hydrophobic interaction between the alkyl beads. In addition, the motion of the molecules is modeled via Langevin dynamics (discussed later). The simulation box is periodic in the X and Y dimensions. To keep a constant simulation volume, reflective boundary conditions are applied to all beads at the side opposite of the z = 0 surface of the simulation box.

All quantities in this study are defined using reduced units.[22] In reduced units, the units of energy, mass, and length are defined so as to save computational costs in simulations and can be easily converted into real units. In this system, the unit of energy is taken as thermal energy, k_BT (k_B is the Boltzmann constant and T is the temperature), which is set to 1. The potential well depth (ε) has units of energy and therefore is specified with respect to k_BT. For instance, an ε = 0.5 implies that the potential well depth is half of the thermal energy. The mass of each bead is set to 1, and the size of each hydrophobic bead (σ) is set to 1 in reduced units. Kindly refer to the authors' previous publication for more details on reduced units.[19]

2.3 | Simulation Details

Langevin dynamics simulations are performed to study adsorption behavior of corrosion inhibitor and oil molecules on the surface. In Langevin dynamics, the motion of molecules is modeled to mimic their interactions with solvent molecules. This is incorporated by applying a Gaussian-distributed random force and a frictional force in the direction opposite of the velocity to the molecules.[22] In these simulations, the temperature of 1.0 and damping constant of 0.1 (time units $[\varepsilon/m\sigma^2]^{0.5}t$) is used.[22] The LJ well-depth parameter for the interaction between hydrophobic beads, ε, is set to 0.065 k_BT. The well depth of the 9-3 potential for interaction between polar head groups and the surface is chosen to be $\varepsilon_S = 5k_BT$. The value of ε was chosen to ensure that hydrophobic interactions between alkyl tails are of the order of thermal energy,[23] and that of ε_S was chosen to match the strong affinity of the polar head group for the metal surface, obtained from density functional theory (DFT) calculations.[24] It has been shown previously that, for ε = 0.065 k_BT, the corrosion inhibitor molecules form a planar or a cylindrical adsorption morophology, depending on the relative size of the polar head bead, on the surface.[20] To study the effect of the length of oil molecules, oil molecules comprised of 10, 19, and 25 alkyl beads per molecule were studied. The length of inhibitor molecules was kept fixed at 20 beads with 1 polar bead and 19 alkyl beads in each molecule. All simulations were performed using the large-scale atomic/molecular massively parallel simulator (LAMMPS) simulations package.[25] For each data point, the simulations were performed in parallel on eight processors or on a graphic processing unit (GPU). Equilibrium was obtained after 3×10^9 to 4×10^9 time-steps.

RESULTS AND DISCUSSION

3.1 | Presence of Oil Molecules Promotes Adsorption

To investigate the effect of oil molecules on adsorption of inhibitor molecules, 400 inhibitor molecules (20 mers) and 400 oil molecules (19 mers) are inserted at random locations in the simulation box. The diameter of the polar head group of inhibitor molecules is $\sigma_p = 2\sigma$. It was shown in the authors' previous study[20] that when $\sigma_p = 2\sigma$, that is, when the polar head is twice the size of a hydrophobic bead, the inhibitor molecules tend to aggregate in cylindrical micelles in the bulk and the adsorbed phases. The size of the simulation box is $27\sigma \times 27\sigma$ in the XY direction and 80σ in the Z direction. As a reference system, the adsorption behavior of 800 inhibitor molecules (and no oil molecules) is first studied. Figure 2(a) shows a representative snapshot of the equilibrium state of the pure inhibitor system. It is observed that the inhibitor molecules with $\sigma_p = 2\sigma$ tend to aggregate in cylindrical micelles on the surface. An enlarged snapshot of the adsorbed film is shown in Figure 2(b). Figure 2(c) shows the distribution of the angle made by the molecular axes of adsorbed molecules with the surface normal, θ. θ = 0° implies that an adsorbed molecule is lying flat on the surface, and θ = –90° means that an adsorbed molecule is "standing" on the surface with the polar group pointing toward the surface. The distribution of θ in Figure 1(c) is non-zero for all values, with higher values close to –60° and +70°, which indicates that the adsorption morphology is like that of a squashed cylinder. Due to the asymmetric geometry of the molecules, the distribution does not peak at ±90°. Such adsorption morphologies have been reported in many atomic force microscopy studies.[26]

Figure 3(a) shows a representative snapshot of the equilibrated system when oil is added to the inhibitors with $\sigma_p = 2\sigma$. Figure 3(b) shows an enlarged image of the adsorbed layer. It is clearly seen that oil molecules are coadsorbed in the inhibitor layer and the cylindrical morphology of the film transforms into a planar morphology. Interestingly, a large number of oil molecules are in the adsorbed layer even though the oil molecules have no affinity for the metal surface. The entrainment of oil molecules is driven by the hydrophobic interactions between inhibitor tails and oil molecules. The distribution of angles (θ) that adsorbed molecules make with the surface normal now has two sharp peaks at ±90° and no value for intermediate angles, indicating that the adsorbed molecules form a planar self-assembled monolayer (SAM). Therefore, a dramatic change in the adsorbed morphology of inhibitor molecules is observed with the introduction of oil molecules, which is a striking result.

Next, the adsorption behavior of inhibitor molecules with $\sigma_p = \sigma$ is discussed. These inhibitor molecules have been

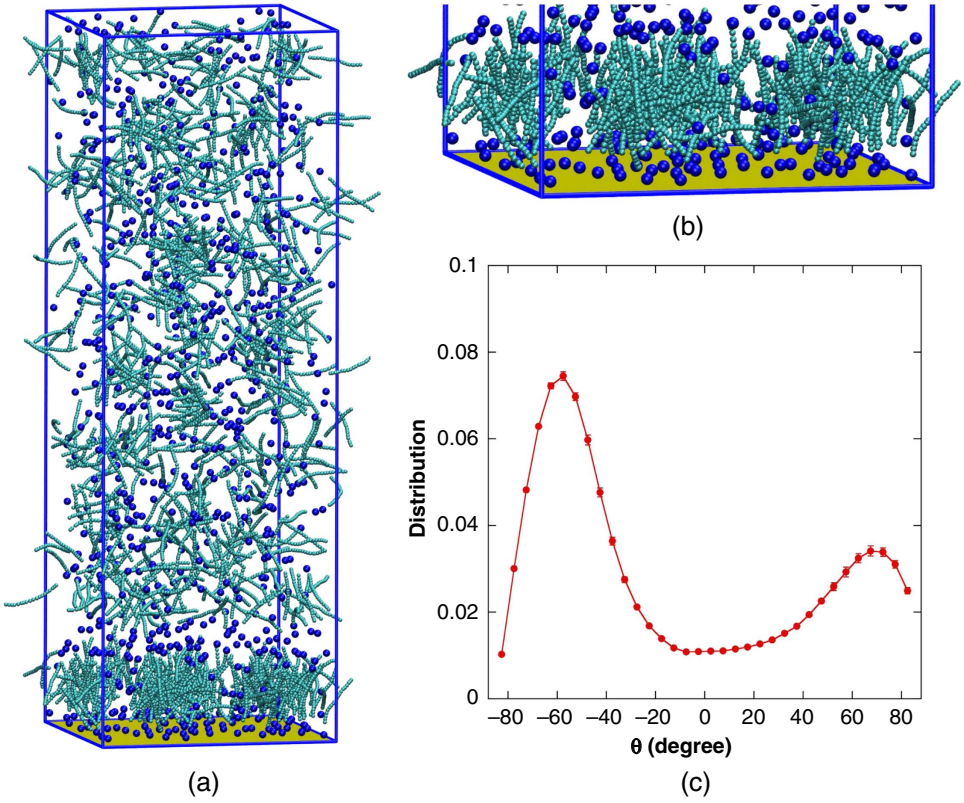

FIGURE 2. *(a) A snapshot of an equilibrium configuration of the pure inhibitor system ($\sigma_p = 2\sigma$). (b) An enlarged snapshot of adsorbed film of the pure inhibitor system ($\sigma_p = 2\sigma$). Blue-colored beads are the polar head groups, and cyan-colored beads are the hydrophobic tails. (c) Distribution of angles (θ) that adsorbed molecules make with the surface.*

shown to form a well-packed planar SAM on the surface.[20] The authors have recently developed a theoretical model that explains the formation of planar SAM in the case of $\sigma_p = \sigma$[27] and that of cylindrical morphologies for $\sigma_p = 2\sigma$.[28] To study the effect of oil molecules on the adsorbed inhibitor film, oil molecules are introduced in the system of inhibitor molecules with $\sigma_p = \sigma$. In these simulations, the simulation box is $20\sigma \times 20\sigma$ in the XY direction and 80σ in the Z direction to keep the volume fraction of the system the same as the $\sigma_p = 2\sigma$ case. 400 inhibitor molecules (20 mers) and 400 oil molecules (19 mers) are randomly inserted into the simulation box. Figure 4(a) shows a representative snapshot of an equilibrium state of the reference system with only inhibitor molecules present. Figure 4(b) shows a snapshot of the system with oil molecules introduced. Both systems show that the adsorbed layer is a SAM. A good fraction of oil molecules gets coadsorbed along with the corrosion inhibitors because of hydrophobic interactions between the oil molecules and the inhibitor tails. Figure 4(c) shows the distribution of θ for the two systems. Both systems show signatures of a planar SAM on the surface.

To quantitatively compare changes in the adsorbed film upon the introduction of oil molecules, the number of molecules adsorbed per unit area (ρ) for $\sigma_p = 2\sigma$ and $\sigma_p = \sigma$ is plotted in Figure 5. For the $\sigma_p = 2\sigma$ case, the addition of oil molecules promotes adsorption. Entrainment of oil molecules transforms the cylindrical morphology of the adsorbed inhibitor film into a planar SAM. This results in a higher concentration of molecules that are tightly packed on the surface. For the $\sigma_p = \sigma$ case, the overall adsorption amount does not change significantly as the inhibitor molecules by themselves are able to adsorb in a tightly packed planar SAM. However, the composition of the adsorbed film changes with a good fraction of oil molecules coadsorbed in the film, even when the oil molecules and the metal surface do not have any attractive interactions in our model.

The simulation results of this study show that oil molecules have a tendency to be coadsorbed in the inhibitor films due to hydrophobic interactions. Interestingly, the entrainment of oil molecules may result in changing the adsorbed morphology of the adsorbed inhibitor film, which can cause enhanced adsorption.

3.2 | Presence of Oil Molecules Improves Corrosion Inhibition Properties of Adsorbed Films

How the structural properties of the adsorbed inhibitor films are affected by the entrainment of oil molecules was also analyzed in this research. The local structural arrangement of molecules in the adsorbed film was studied by calculating the radial distribution function (RDF) along the plane of the film, the XY plane, RDFxy(r). RDFxy(r) shows the local density of molecules around a given molecule divided by the density expected for a uniform distribution. Therefore, RDFxy(r) = 1 implies that there is no preferential arrangement of molecules (ideal gas behavior).

Figure 6(a) shows the RDFxy(r) of adsorbed molecules for the pure inhibitor system and for the inhibitor + oil system for the $\sigma_p = 2\sigma$ case. The RDFxy(r) of the inhibitor-only system shows a peak and a shoulder followed by a depletion region, indicating that the molecules are aggregated in micellar structures. On the other hand, for the inhibitor + oil system, the RDFxy(r) shows regular peaks, indicating the presence of a much more ordered structure in the film reminiscent of a SAM. For the $\sigma_p = \sigma$

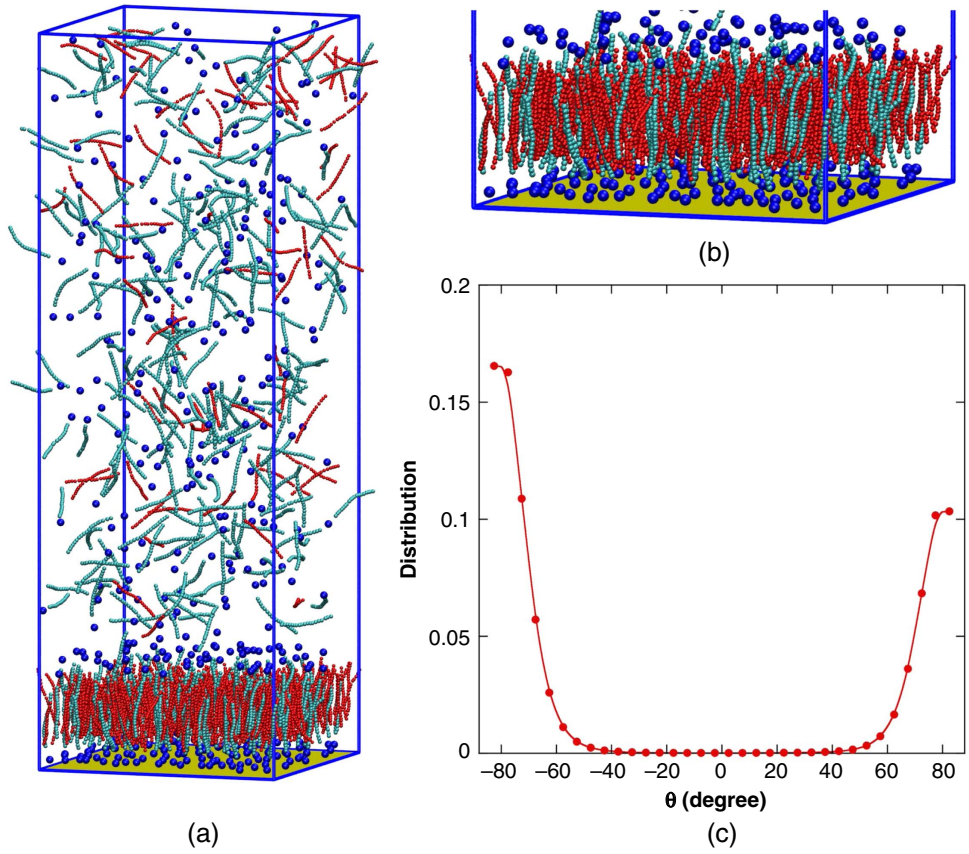

FIGURE 3. *(a) A snapshot of an equilibrium configuration of the inhibitor + oil system ($\sigma_p = 2\sigma$). (b) An enlarged snapshot of configuration of the inhibitor + oil system ($\sigma_p = 2\sigma$). Blue-colored beads are the polar head groups, cyan-colored beads are the hydrophobic tails, and the red-colored beads represent the oil molecules. (c) Distribution of angles (θ) that adsorbed molecules make with the surface.*

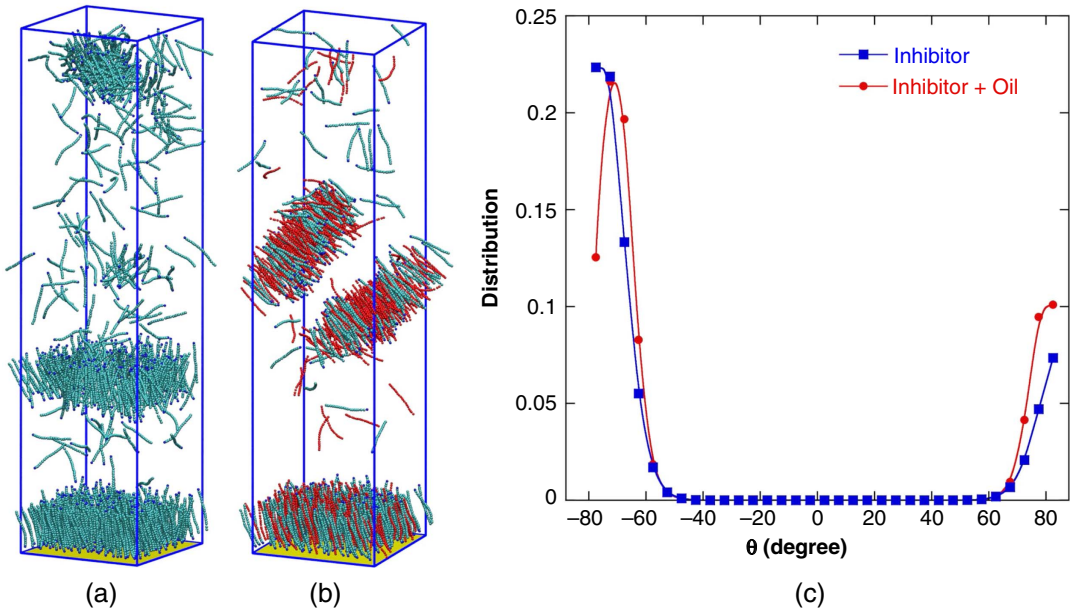

FIGURE 4. *(a) A snapshot of an equilibrium configuration of the pure inhibitor system ($\sigma_p = \sigma$). (b) A snapshot of an equilibrium configuration of the inhibitor + oil system ($\sigma_p = \sigma$). Oil molecules are in red, and inhibitor molecules are in cyan with a blue-colored polar head group. (c) Distribution of angles (θ) that adsorbed molecules make with the surface for $\sigma_p = \sigma$ with oil and without oil molecules present.*

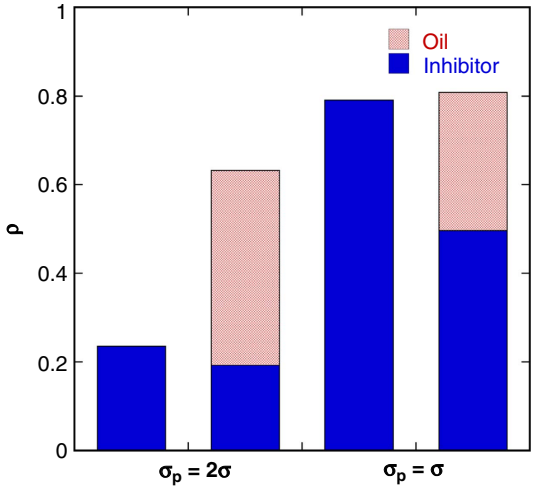

FIGURE 5. *Number of molecules adsorbed per unit area, ρ, for $\sigma_p = 2\sigma$ and $\sigma_p = \sigma$ with oil and without oil molecules present. Error is of the order 10^{-4}.*

case (Figure 6[b]), the RDFxy(r) of the pure inhibitor system shows regular peaks, a signature of an ordered SAM. Interestingly, for the inhibitor + oil system, the peaks of the RDFxy(r) become larger, indicating that, in the presence of oil molecules, the film becomes more ordered.

It is understood that adsorbed inhibitor films form a hydrophobic barrier over the metal surface and mitigate corrosion. Thus, a larger hydrophobic barrier of the films is preferable. A simple molecular measure of film hydrophobicity can be defined as the fraction of adsorbed molecules (inhibitor and oil) with their alkyl groups exposed to the solution. Figure 7 shows film hydrophobicity for $\sigma_p = 2\sigma$ and $\sigma_p = \sigma$ for the systems with and without oil molecules. It is seen that, in a pure inhibitor system, film hydrophobicity is around 0.7, indicating that about 70% of the molecules are adsorbed with their polar head group pointing toward the surface. It is often presumed that a SAM layer of adsorbed molecules forms a uniformly hydrophobic layer. Contrary to this, simulations in this study show that the adsorbed film of inhibitor molecules is patchy with some fraction of polar groups toward the solution. The film hydrophobicity increases to approximately 0.9 with the addition of oil molecules.

The above results show that the entrainment of oil molecules changes the properties of adsorbed films, making them structurally more ordered and more hydrophobic. Thus, these simulation results indicate that the efficiency of corrosion inhibitors should increase when the adsorbed inhibitor films are exposed to oil.

3.3 | Effect of Length of Oil Molecules

In reality, oil molecules in contact with an inhibitor in an aqueous environment are of different molecular sizes. In this section, the results of how the length of oil molecules affects the entrainment behavior are discussed. In these simulations, oil molecules with three different tail lengths, comprising of 10, 19, and 25 beads, are compared (named as oil10, oil19, and oil25). The polar head group size is set to $\sigma_p = \sigma$. The simulation box is $20\sigma \times 20\sigma$ in the XY direction and 80σ in the Z direction. 400 inhibitor molecules (20 mers) and 400 oil molecules are randomly inserted into the simulation box.

Figure 8 shows the total number of molecules adsorbed on the surface at equilibrium. In the system with oil10 and oil19 molecules, the equilibrium adsorption amount is comparable to the pure inhibitor case. However, in the system with oil25 molecules, the total number of adsorbed molecules decreases. This decrease in adsorption is due to aggregation of oil molecules in the bulk phase. With longer tail lengths, the overall interaction between the tails of inhibitor molecules and the oil molecules is stronger, which results in aggregation in the bulk. Although the oil10 and the oil19 systems have similar total adsorption amounts, the composition of the adsorbed film is different. Smaller oil molecules have lower hydrophobic interactions, and therefore fewer number of oil10 molecules are coadsorbed in the corrosion inhibitor layer in comparison to the oil19 system.

3.4 | Experimental Confirmation

In 2018, a proprietary project at the Institute of Corrosion and Multiphase Technology (ICMT) was conducted concurrently

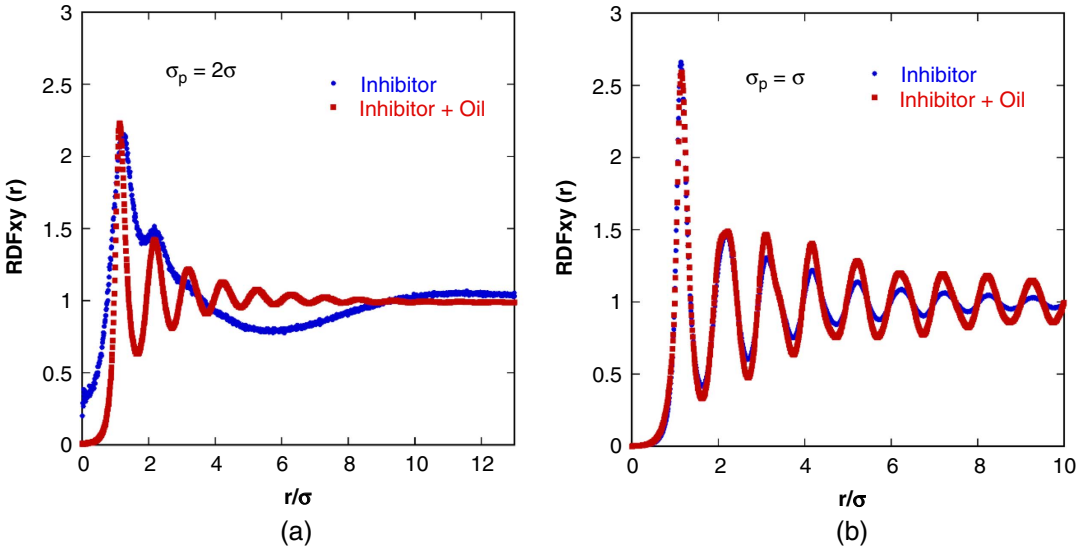

FIGURE 6. *Radial distribution function in the XY plane, RDFxy(r), of adsorbed molecules in a pure inhibitor system (blue) and in an inhibitor + oil system (red) for (a) $\sigma_p = 2\sigma$ and (b) $\sigma_p = \sigma$.*

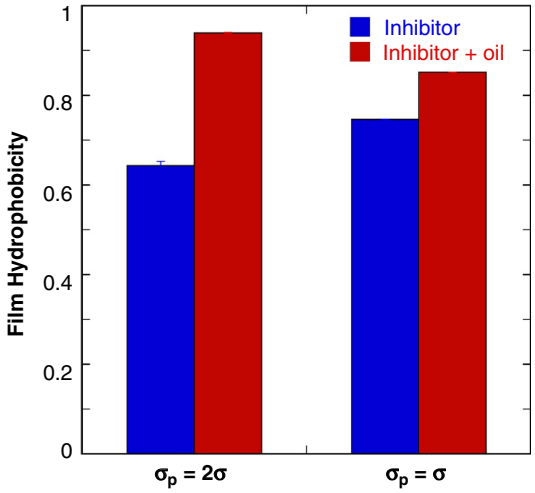

FIGURE 7. *Comparison of film hydrophobicity for $\sigma_p = 2\sigma$ and $\sigma_p = \sigma$ with oil and without oil molecules present.*

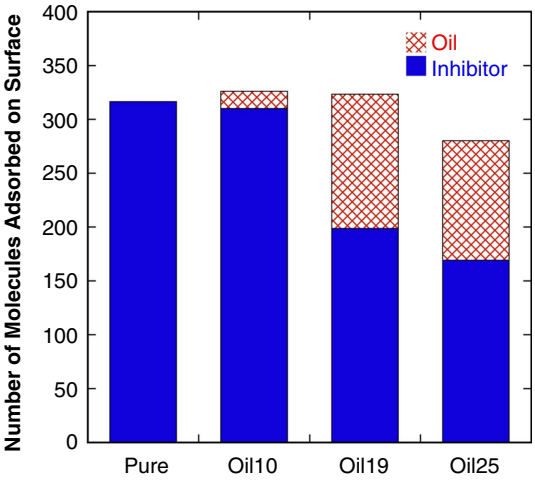

FIGURE 8. *Number of inhibitor molecules adsorbed on the surface for a pure inhibitor system, or with oil of molecular lengths of 10, 19, and 25.*

with the abovementioned molecular simulations, which focused on comparison of testing methodology, inhibitor efficiency, and inhibitor adsorption/desorption. Information from laboratory testing of a commercial inhibitor (henceforth referred to as proprietary corrosion inhibitor), with and without the presence of hydrocarbon, is provided for tests focused on efficiency and persistence under a specific set of environmental conditions.

In order to test the influence of a hydrocarbon on the efficiency and persistence of corrosion inhibitors, one set of tests was completed without a hydrocarbon present, and the second set of tests contained a 1,000-ppm concentration (2 mL) of LVT 200[†] oil (LVT 200 is a hydrotreated light distillate which is a colorless, clear model oil that has a specific gravity of 0.82 to 0.83, 41.5 American Petroleum Institute [API] gravity, with a hydrocarbon chain of C9 to C16) added on top of the 2 L of brine used in each experiment. Each experiment was conducted using a test configuration as shown in Figure 9. The system was

[†] Trade name.

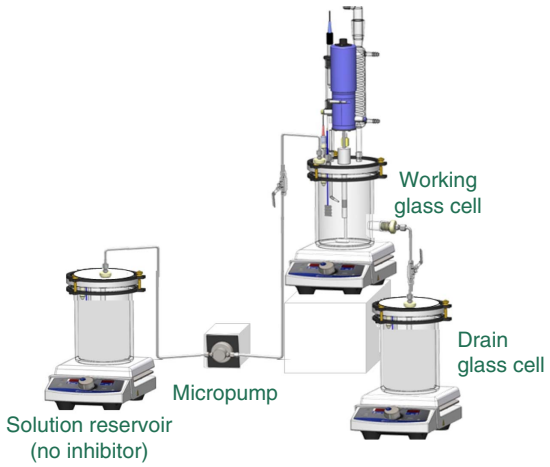

FIGURE 9. *Experimental configuration for testing inhibitor efficiency and persistence.*

designed so that a CO_2-purged brine could be pumped from the solution reservoir to the working cell and gravity drained into a CO_2 purged cell. Operating procedures were developed so that the working electrode (rotating cylinder electrode, RCE) would always remain 100% wetted and never come into direct contact with the oil layer (if present) on top of the brine. The brine, with an ionic strength of 0.5 and temperature of 80°C, was sparged in both glass cells with CO_2 for 2 h prior to the test to remove oxygen. The brine in both glass cells was adjusted to a pH of 6.0 using 1 M $NaHCO_3$ during the deoxygenation.

Corrosion rate testing was conducted with a mild steel RCE in the 2 L "working glass cell" (Figure 9). The RCEs were made from an API 5 L X65 material; each had dimensions of 12 mm outside diameter × 14 mm height, were polished to a 600-grit finish, and were cleaned in an ultrasonic isopropyl alcohol bath before the tests. In each experiment, the RCE was placed into the glass cell with the purged brine, the CO_2 purged LVT 200 oil was injected on top of the brine (if used), and then rotation was set at approximately 4,000 rpm for a 20 Pa wall shear stress (WSS). Electrochemical connections were made to conduct linear polarization resistance (LPR) measurements for corrosion rate, and electrochemical impedance spectroscopy (EIS) measurements were used to determine solution resistance.

The small amount of oil injected on top of the solution would be partially dispersed into the solution as small droplets at the high rotational speed, but they would immediately separate and return to the top of the solution when the rotation was stopped. Experiments conducted without an inhibitor added showed no influence of the dispersed LVT oil on the baseline corrosion rate as compared to similar experiments with no inhibitor and no LVT oil present.

EIS measurements were performed at the open-circuit potential (OCP) using a potential perturbation with an amplitude of 10 mV root mean squared at a frequency range between 1 Hz and 5 kHz to determine the solution resistance at the beginning of each experiment. Polarization resistance was obtained from LPR. The working electrode was polarized from −5 mV to +5 mV with respect to the OCP at a scan rate of 0.125 mV/s with a sampling period of 2 s. Then, the charge transfer resistance (R_{CT}) was obtained by subtracting the solution resistance from the polarization resistance.

Subsequently, corrosion current densities (i_{corr}) were obtained by using a classical Stern-Geary equation, resulting in:[29]

$$i_{corr} = \frac{B}{R_{CT}} \quad (6)$$

where B is a constant (26 mV/decade for CO_2 corrosion). The current density was then converted into mm/y by using Faraday's law.[30] In the case of the steel corrosion (iron dissolution), the corrosion rate is CR (mm/y) = 1.159 i_{corr}.

Each test began with 4 h of precorrosion with or without the presence of oil. Electrochemical measurements were started within 10 min after the RCE was inserted into solution, as soon as the OCP became stable. After the last LPR measurement for the 4 h precorrosion, the commercial inhibitor was injected on top of the solution for a 100 ppm concentration in the total liquid volume. Each test then continued for an additional 20 h to observe the decreasing trend of the corrosion rate until a steady-state corrosion rate was obtained. The data from this part of the test would be used to focus on inhibitor adsorption and inhibitor efficiency. At 20 h, the RCE was stopped, stir bar rotation was started in the cell to maintain a fully mixed solution, and increments of approximately 200 mL of brine would be drained and refilled in the working glass cell to achieve a 5 ppm concentration of inhibitor while keeping the RCE continuously water wetted but never directly exposed to the oil layer. The change in inhibitor concentration by this dilution procedure was calculated based on assuming a fully mixed solution after each step in the dilution process. After the drain and refill procedure was complete, which required about 5 min, the stir bar was stopped and RCE returned to the 20 Pa WSS setting. Electrochemical measurements for LPR were then continued until a stable corrosion rate was achieved (ΔCR < ±0.002 mm/y). The data from this part of the test would focus on inhibitor persistence and final corrosion rate. Each test, with and without a hydrocarbon present, was repeated twice, and the results shown in Figures 10 and 11 represent the average of the two experiments with appropriate error bars.

The data for the proprietary corrosion inhibitor tests are shown in Figures 10 and 11, and the composition as provided in the material safety data sheet (MSDS) is shown in Table 1.

The data in Figure 10 show the trend for the addition of the proprietary corrosion inhibitor. Without the hydrocarbon present, the addition of the inhibitor provided a corrosion inhibition efficiency of 99.88%. The average corrosion rate

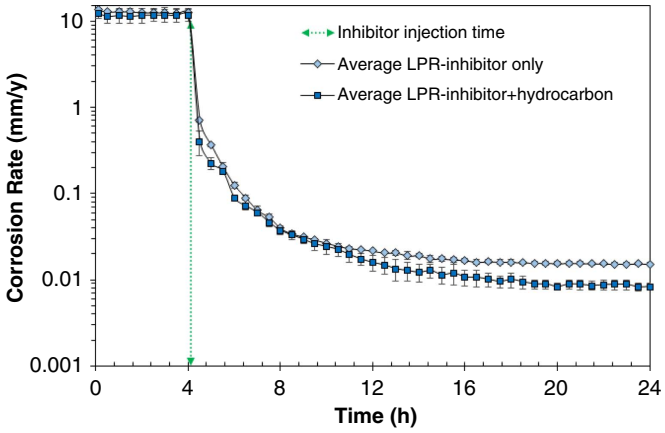

FIGURE 10. *Inhibitor adsorption experiments conducted with and without the presence of a hydrocarbon (80°C, pH 6.0, 0.5 ionic strength brine, RCE at 20 Pa WSS, 1,000 ppm LVT 200).*

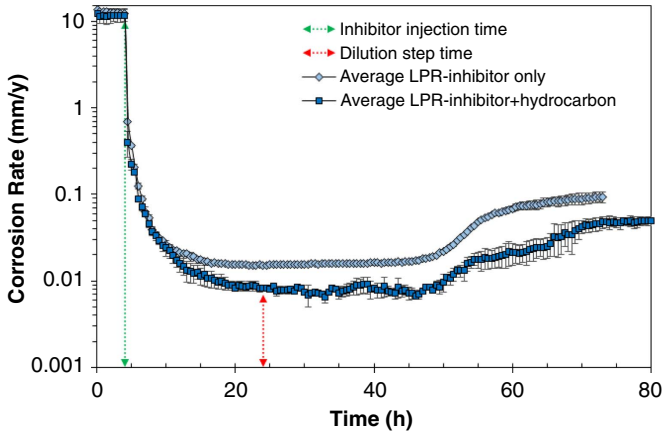

FIGURE 11. *Inhibitor adsorption and dilution experiments conducted with and without the presence of a hydrocarbon (80°C, pH 6.0, 0.5 ionic strength brine, RCE at 20 Pa WSS, 1,000 ppm LVT 200).*

Table 1. *Proprietary Corrosion Inhibitor MSDS Listed Components*

Inhibitor Components	% content
Methanol	30%–60%
Substituted aromatic amine	10%–30%
Quaternary ammonium compound 1	10%–30%
Fatty acid	5%–10%
Quaternary ammonium compound 2	5%–10%
2-mercaptoethanol	5%–10%
Diethanolamine	1%–5%
Isopropanol	1%–5%
Oxyalkylate	1%–5%
Heavy aromatic naphtha	1%–5%
Naphthalene	0.1%–1%

during precorrosion for the experiments without hydrocarbon was 12.4±1.6 mm/y and the inhibited corrosion rate was 0.015±0.001 mm/y. With the hydrocarbon present, the addition of inhibitor provided a corrosion inhibition efficiency of 99.93%. The average corrosion rate during precorrosion for the experiments with hydrocarbon was 11.7±1.9 mm/y and the inhibited corrosion rate was 0.008±0.001 mm/y. Although the final inhibited corrosion rate without the presence of a hydrocarbon was already low (0.015±0.001 mm/y), the addition of LVT 200 to the system further decreased the corrosion rate to 0.008±0.001 mm/y.

The data in Figure 11 show both the addition and dilution parts of the full experiment. The dilution procedure was performed to obtain approximately 5 ppm of proprietary corrosion inhibitor. The final corrosion rate after dilution to 5 ppm for experiments without hydrocarbon was 0.093±0.013 mm/y, while in those same types of tests with hydrocarbon present, it was lower approximately by a factor of two: 0.049±0.006 mm/y. In terms of inhibitor efficiency, the experiment with hydrocarbon had a 99.58% efficiency as compared to a 99.25% efficiency without hydrocarbon present.

Persistence of the inhibitor in these tests was defined by when the corrosion rate began increasing much more than the

random variation of the stable corrosion rate measured before the dilution procedure. For the proprietary corrosion inhibitor, the persistence of the inhibitor without hydrocarbon present was about 22 h while the persistence of the inhibitor with hydrocarbon present was about 26 h. One can also argue that both tests with the proprietary corrosion inhibitor showed a continued persistence as previous tests with the addition of only 5 ppm of the proprietary corrosion inhibitor had a stable corrosion rate of 0.140±0.001 mm/y after 20 h. This could also be an indication of the precision of the dilution procedure, which is very similar in the tests with no hydrocarbon, where the tests with hydrocarbon could indicate that some influence of a partitioning equilibrium between the oil phase and the solution occurred.

CONCLUSIONS

➢ Previous experimental results have shown that the addition of oil molecules can reduce the corrosion rate by enhancing the efficiency of an inhibitor film, although these tests did not provide any molecular-level understanding of why and how these oil molecules influence corrosion inhibitor adsorption for mitigation of corrosion. In this study, the authors have used molecular simulations to study how oil molecules affect adsorption behavior and characteristics of adsorbed inhibitor films. It was found that, even though oil molecules do not interact with the metal surface, they can be coadsorbed in the inhibitor layer because of lateral hydrophobic interactions between the oil molecules and the alkyl tails of inhibitor molecules. In addition, an interesting morphological transition was observed in the adsorbed films wherein cylindrical micelles of adsorbed inhibitors get transformed into planar SAMs. This transition results in a significant increase in the adsorption of molecules on the surface. Different lengths of oil molecules have different coadsorption tendencies. Large oil molecules lead to aggregation of molecules in the bulk phase, thereby reducing adsorption, while smaller oil molecules have little tendency to be coadsorbed in the inhibitor film. Oil molecules that are comparable in length to the alkyl tail of inhibitor molecules have a strong tendency to coadsorb with the inhibitor molecules. These experiments have revealed that the presence of a hydrocarbon phase is beneficial in corrosion mitigation for a commercial inhibitor. In the experiments, the inhibitor layer adsorbed at the metal surface would be expected to contain some of the hydrocarbon phase because of the increase in the final inhibition efficiency. As the molecular model is focused on the diffusion boundary layer right next to the metal surface, the mechanisms portrayed by the molecular model are confirmed to be correct.

ACKNOWLEDGMENTS

This work was supported by the NSF CBET grant 1705817. The experiments were performed as part of a proprietary British Petroleum (BP) project at the Institute of Corrosion and Multiphase Technology (ICMT) that focused on comparison of testing methodology, inhibitor efficiency, and inhibitor adsorption/desorption, which produced a proprietary document: J. Dominguez Olivo, C. Prieto, B. Brown, S. Nesic, Testing Methodology for Inhibitor Evaluation, Proprietary testing on inhibitor persistency. Since the project also included the testing of commercial inhibitors in the presence of oil, permission for publication was requested and was granted by the proprietary project lead at BP, Will Durnie, who is the principal corrosion engineer of BP with research focus on inhibitor use, efficiency, and persistence. The authors are grateful to BP for granting the permission to include these experimental results in this publication. The authors also thank researchers at the ICMT for useful discussions. XK thanks the support of the Ohio University Graduate College Fellowship for the year 2018–2019. Computational resources for this work were provided by the Ohio Supercomputer Center and NSF XSEDE grant DMR190005.

CONFLICT OF INTEREST

The authors declare no conflicts of interest.

DATA AVAILABILITY STATEMENT

The raw and processed data required to reproduce these findings are available to download from https://data.mendeley.com/datasets/3x6xm4tdm3/1. Molecular simulation trajectory files are not available for download because their size is more than 100 GB.

References

1. M.B. Kermani, A. Morshed, *Corrosion* 59, 8 (2003): p. 659-683.
2. A.J. McMahon, *Colloid Surf.* 59 (1991): p. 187-208.
3. M. Finšgar, J. Jackson, *Corros. Sci.* 86 (2014): p. 17-41.
4. J.A. Martin, F.W. Valone, *Corrosion* 41, 5 (1985): p. 281-287.
5. Y. Duda, R. Govea-Rueda, M. Galicia, H.I. Beltrán, L.S. Zamudio-Rivera, *J. Phys. Chem. B* 109, 47 (2005): p. 22674-22684.
6. A. Edwards, C. Osborne, S. Webster, D. Klenerman, M. Joseph, P. Ostovar, M. Doyle, *Corros. Sci.* 36, 2 (1994): p. 315-325.
7. M.N. Shalaby, M.M. Osman, *Anti-Corros. Methods Mater.* 48 (2001): p. 309-318.
8. G. Zhang, C. Chen, M. Lu, C. Chai, Y. Wu, *Mater. Chem. Phys.* 105, 2-3 (2007): p. 331-340.
9. I. Jevremović, M. Singer, S. Nešić, V. Mišković-Stanković, *Corros. Sci.* 77 (2013): p. 265-272.
10. I. Jevremović, M. Singer, S. Nešić, V. Mišković-Stanković, *Mater. Corros.* 67, 7 (2016): p. 756-768.
11. J.D. Olivo, B. Brown, D. Young, S. Nešić, *Corrosion* 75, 2 (2019): p. 137-139.
12. Y. Kurapati, S. Sharma, *J. Phys. Chem. B* 122 (2018): p. 5933-5939.
13. H. Singh, S. Sharma, *J. Phys. Chem. B* 124, 11 (2020): p. 2262-2267.
14. C. Li, S. Richter, S. Nešić, *Corrosion* 70, 9 (2014): p. 958-966.
15. Y. Chen, W.P. Jepson, *Electrochim. Acta* 44, 24 (1999): p. 4453-4464.
16. M. Foss, E. Gulbrandsen, J. Sjöblom, *Corrosion* 64, 12 (2008): p. 905-919.
17. M. Foss, E. Gulbrandsen, J. Sjoblom, *Corrosion* 65, 1 (2009): p. 3-14.
18. M. Foss, E. Gulbrandsen, J. Sjoblom, *Corrosion* 66, 2 (2010): p. 025005-025005-11.
19. S. Sharma, X. Ko, Y. Kurapati, H. Singh, S. Nešić, *Corrosion* 75, 1 (2019): p. 90-105.
20. X. Ko, S. Sharma, *J. Phys. Chem. B* 121, 45 (2017): p. 10364-10370.
21. J.D. Weeks, D. Chandler, H.C. Andersen, *J. Chem. Phys.* 54, 12 (1971): p. 5237-5247.
22. M.P. Allen, D.J. Tildesley, *Computer Simulation of Liquids* (Oxford, United Kingdom: Oxford University Press, 1989).
23. N. Choudhury, B.M. Pettitt, *J. Am. Chem. Soc.* 127, 10 (2005): p. 3556-3567.
24. N. Kovačević, I. Milošev, A. Kokalj, *Corros. Sci.* 124 (2017): p. 25-34.
25. S. Plimpton, *J. Comput. Phys.* 117, 1 (1995): p. 1-19.
26. M. Jaschke, H.-J. Butt, H.E. Gaub, S. Manne, *Langmuir* 13, 6 (1997): p. 1381-1384.
27. S. Sharma, H. Singh, X. Ko, *J. Phys. Chem. B* 123, 34 (2019): p. 7464-7470.
28. X. Ko, S. Sharma, *J. Phys. Chem. B* 124, 26 (2020): p. 5517-5524.
29. W.J. Lorenz, F. Mansfeld, *Corros. Sci.* 21, 9-10 (1981): p. 647-672.
30. J. Newman, K.E. Thomas-Alyea, *Electrochemical Systems* (Hoboken, NJ: John Wiley & Sons, 2012).